Computed Spectroscopy using Segmented Apertures

Ralph T. Hoctor*[a], Frederick W. Wheeler[a] and Eamon B. Barrett[b]
[a]General Electric Global Research, 1 Research Circle, Niskayuna, NY, USA 12309;
[b]Lockheed Martin Space Systems, ATC, 1111 Lockheed Martin Way, Sunnyvale, CA, USA 94089

ABSTRACT

A novel technique for imaging spectroscopy is introduced. The technique makes use of an optical imaging system with a segmented aperture and intensity detector array on the imaging plane. The point spread function (PSF) of such a system can be adjusted by modifying the path lengths from the subapertures to the image plane, and the shape of the resulting point spread function will vary as a function of wavenumber. An image reconstruction approach is taken to convert multiple recorded pan-chromatic images with different wavenumber-varying point spread functions into a hyperspectral data set. Thus, the technique described here is a new form of computed imaging.

Keywords: imaging spectroscopy, hyperspectral imaging, synthetic aperture imaging, segmented apertures.

1. INTRODUCTION

In this paper we describe a new approach to imaging spectroscopy using a pan-chromatic imaging system with an adjustable point spread function (PSF). This approach is an image reconstruction technique, in which a collection of blurred pan-chromatic images of a scene is used to compute a single, spatially sharp, hyperspectral image (HSI). Since this is clearly a new form of computed imaging, we have given it the name *Computed Spectroscopy* (CS).

An HSI is a data set composed of multiple planar images, corresponding to a range of contiguous wavenumber bands having an average spacing in wavelength of about 10nm. Such a data set typically extends in wavelength from 400 to 2400 nm [1]. Hyperspectral images are often collected by airborne or orbital imaging spectroscopy instruments for remote sensing applications, and use either a prism, diffraction grating or Michelson interferometer to produce the wavenumber spectrum at each pixel. A new approach was recently proposed by Kendrick, et al. [2,3,4] using a division-of-wavefront interferometer implemented using a segmented aperture. The method of [2,3] divides the segmented aperture into two parts, each composed of multiple subapertures, varies their relative path length to the image plane and converts the resulting interferogram to an HSI using Fourier Transform Imaging Spectroscopy (FTIS). The CS method can be applied to the same aperture, but adopts a spatial frequency domain computational approach that allows all of the aperture segments to be used independently. The method of [2,3] also requires a spatial filtering operation that low-pass filters each wavenumber plane, limiting the spatial frequencies in the image to a range smaller than that passed by the aperture, while the method of this paper has no such limitation, and produces higher spatial resolution images. Additionally, the present approach provides an interesting theoretical connection between image restoration, incoherent aperture synthesis and interferometric spectroscopy.

In this paper we introduce the Computed Spectroscopy approach in the context of a segmented aperture for which the distance of each subaperture to the image plane can be finely adjusted, as in [2,3]. This produces the effect of applying a wavenumber-varying phase weight to each subaperture. Such an aperture provides a specific approach to implementing the required adjustable PSF, but the method is not limited to this particular hardware implementation. Segmented aperture systems have long been considered for incoherent synthetic aperture imaging [5, chapter 36]. The result of each subaperture adjustment is a distinct PSF that changes both its size and shape as a function of wavenumber.

This technique, and any other that performs imaging spectroscopy using a division-of-wavefront approach, suffers from an inability to estimate the wavenumber spectra for spatial frequencies near the origin. This paper gives an explanation of this effect and shows how the segmented aperture can be structured to mitigate it. The analysis given here makes use of the coarray concept [6,7] from the field of Array Signal Processing, where array apertures composed of multiple elements are commonplace.

* hoctor@research.ge.com

This paper is structured as follows. The next section will cover the image formation model. Section 3 will introduce the algebraic reconstruction method for Computed Spectroscopy and the numerical solution of the problem. Section 4 discusses the rank of the system to be inverted in the image reconstruction problem as a function of spatial frequency. In Section 5, we give some simulation results to illustrate the method. In Section 6 we conclude and give some directions for future work.

2. SEGMENTED APERTURE IMAGING SYSTEMS.

Our application is imaging of a reflecting/absorbing object illuminated by sunlight, and we use the standard model of an incoherent imaging system and a scalar wavefield [8]. We will take the source distribution to be in the far field of the aperture and the image plane to lie at the focal distance of the aperture optics. The observed intensity distribution on the image plane is digitized using a 2-D detector array.

Segmented aperture imaging systems allow a change of the imaging PSF from image to image by the adjustment of path lengths between the subapertures and the image formation plane. It should be noted that, even though we assume incoherent imaging, we depend on the coherent combination of the wavefields from the various subapertures on the image plane to form the PSF. That is, all the optical path length differences between the subapertures must be less than the coherence interval of the wavefield. The recorded image is the intensity of this coherent combination of wavefields.

The PSF is the Fourier transform of the transmittance of the aperture. We denote the narrowband aperture transmittance function of an N-aperture system by the sum of the transmittances of the individual, spatially disjoint subapertures:

$$\Phi(\mathbf{u};k) = \sum_{n=1}^{N} \Phi_n(\mathbf{u};k) \tag{1}$$

where $k = 2\pi/\lambda$ is the scalar wavenumber associated with the optical center frequency. The aperture transmittance function is parameterized by k, because it is implemented by imposing delays (longer path lengths) on the wavefield that vary by subaperture. A path length difference of Δ results in a phase difference of $\exp(jk\Delta)$, and if we interpret this as imposing a phase-only weight on a subaperture, then that weight clearly varies with wavenumber. This type of array can be seen as the optical analog of the delay-and-sum beamformer used in passive, broadband acoustical imaging [7].

The narrowband PSF is given by

$$\begin{aligned} P(\mathbf{x};k) &= \left| \int_A \Phi(\mathbf{u};k)\, e^{\frac{-jk}{z}\mathbf{u}^T\mathbf{x}}\, d\mathbf{u} \right|^2 \\ &= \int_{CA} \left[\int_A \Phi(\mathbf{u};k)\, \Phi^*(\mathbf{u}-\mathbf{w};k)\, d\mathbf{u} \right] e^{\frac{-jk}{z}\mathbf{w}^T\mathbf{x}}\, d\mathbf{w} \\ &= \int_{CA} C(\mathbf{w};k)\, e^{\frac{-jk}{z}\mathbf{w}^T\mathbf{x}}\, d\mathbf{w} \end{aligned} \tag{2}$$

where $\mathbf{u}$ is a vector variable representing location on the aperture plane, $\mathbf{u}^T\mathbf{x}$ is an inner product of $\mathbf{u}$ and $\mathbf{x}$, the symbol A is used as the limit of integration to represent integration over the aperture plane, the symbol CA represents integration over the coarray, defined below, and the quantity z represents the distance between the aperture plane and the image plane. (We will use the term *optical Fourier transform* when the complex exponential kernel of the transform contains the wavenumber and image plane distance as in (2), and the term *spatial Fourier transform* when it does not.) Eq (2) expresses the narrowband PSF as the optical Fourier transform of the autocorrelation, $C(\mathbf{w};k)$, of the aperture transmittance function, which is also defined in (2). This is a well-known result in optics [8]. For the segmented aperture we can express the autocorrelation function defined in (2) as

$$C(\mathbf{w};k) = \sum_{n=1}^{N} \sum_{m=1}^{N} C_{n,m}(\mathbf{w};k) \tag{3}$$

where $C_{n,m}(\mathbf{w};k)$ is the cross-correlation of $\Phi_n(\mathbf{u};k)$ and $\Phi_m(\mathbf{u};k)$, given in (1).

We can express $\widetilde{P}(\mathbf{v};k)$, the inverse spatial Fourier transform of the PSF, in terms of $C(\mathbf{w};k)$ using (2) by writing

$$\widetilde{P}(\mathbf{v};k)=\int_{\infty} P(\mathbf{x};k)\, e^{j2\pi \mathbf{v}^T\mathbf{x}}\, d\mathbf{x}=\int_{CA} C(\mathbf{w};k)\left[\int_{\infty} e^{-j2\pi\left(\frac{\mathbf{w}}{\lambda z}-\mathbf{v}\right)^T\mathbf{x}}\, d\mathbf{x}\right] d\mathbf{w}=C(\lambda z\mathbf{v};k) \tag{4}$$

(The integral in brackets evaluates to a delta function.) The function $C(\lambda z\mathbf{v};k)$ in (4) is simply the unnormalized optical transfer function (OTF).

The coarray is defined as the support in the **w**-plane of the autocorrelation function $C(\mathbf{w};k)$; the support of this function does not vary with k, but its value does, in general. Integration over the coarray is denoted by the limit of integration CA in (2) and (4). We refer to the variable **w** as a *lag*, and the support regions of the subaperture correlations, $C_{n,m}(\mathbf{w};k)$, will be referred to as *coarray segments*. Each coarray segment is centered at a location on the coarray plane that is the vector location difference between the area centroids of the correlated subapertures; we call this location the *lag* of that segment. In the present work we will consider the aperture geometry depicted in Figure 1a, which is composed of N=9 annular segments [3]. The coarray segments associated with this aperture are depicted in Figure 1b. Each circle in Figure 1b is of radius 2R, where R is the outer radius of the annular subapertures depicted in Figure 1a, and there are $\frac{N(N-1)}{2}+1=37$ of them. Figure 1c depicts a single subaperture shape and its autocorrelation (assuming no apodization). The aperture shape is shown on the top, and the silhouette of the autocorrelation is shown in the bottom. The autocorrelation is rotationally symmetric, and the peak value is proportional to the area of the aperture.

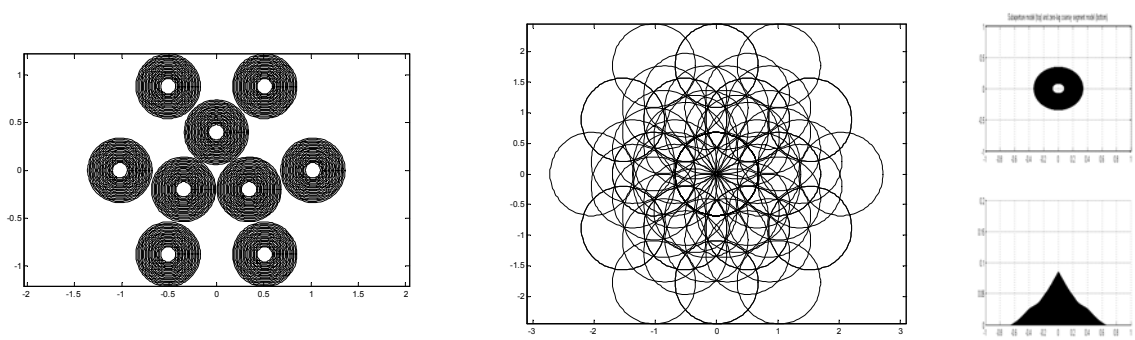

Figure 1: a) array geometry, b) locations of coarray segments, c) subaperture autocorrelation.

The intensity image due to a monochromatic wavefield with wavenumber k is given by the convolution of the PSF at k with S(**x**, k), the narrowband intensity source distribution, which is a function both of location on the source plane and wavenumber. Expressing this convolution in the Fourier transform domain and using (4) gives

$$I(\mathbf{x};k)=\int_{CA_{\lambda z}} C(\lambda z\mathbf{v};k)\,\widetilde{S}(\mathbf{v},k)\, e^{-j2\pi\,\mathbf{v}^T\mathbf{x}}\, d\mathbf{v} \tag{5}$$

where $\widetilde{S}(\mathbf{v};k)$ is the inverse spatial Fourier transform of the source, $S(\mathbf{x},k)$ and the limit of integration $CA_{\lambda z}$ represents integration over the image of the coarray in the spatial frequency domain under the mapping $\mathbf{v}=\mathbf{w}/\lambda z$. In the spatial frequency domain $CA_{\lambda z}$ is the support of the inverse spatial transform of the narrowband PSF at wavelength λ.

3. COMPUTED SPECTROSCOPY USING SEGMENTED APERTURES.

The computed spectroscopy algorithm works by processing multiple pan-chromatic images. In order to discuss it, we will describe the observed pan-chromatic images that are formed to provide input to the computation. We model the observed panchromatic image as the integral over the optical passband in wavenumber of the monochromatic image defined by (5):

$$I(\mathbf{x}) = \int_K I(\mathbf{x}; k)\, dk \tag{6}$$

We have assumed here that the response of the imaging system is uniform over the its passband in the wavenumber domain, which we denote by K; however, it would also be easy to account for a wavenumber-dependent sensitivity in the system. We denote the spatial Fourier transform of (6) by:

$$\tilde{I}(\mathbf{v}) = \int_\infty \int_K I(\mathbf{x}; k)\, e^{j2\pi \mathbf{x}^T \mathbf{v}} dk\, d\mathbf{x} \tag{7}$$

Substituting (5) into (7) gives

$$\begin{aligned}\tilde{I}(\mathbf{v}) &= \int_K \int\int_{CA_{\lambda z}} C(\lambda z \boldsymbol{\omega}; k)\, \tilde{S}(\boldsymbol{\omega}, k)\, e^{-j2\pi \boldsymbol{\omega}^T \mathbf{x}}\, d\boldsymbol{\omega}\, e^{j2\pi \mathbf{v}^T \mathbf{x}}\, d\mathbf{x}\, dk \\ &= \int_K \int_{CA_{\lambda z}} C(\lambda z \boldsymbol{\omega}; k)\, \tilde{S}(\boldsymbol{\omega}, k) \left[\int e^{-j2\pi (\boldsymbol{\omega} - \mathbf{v})^T \mathbf{x}}\, d\mathbf{x} \right] d\boldsymbol{\omega}\, dk \\ &= \int_K C(\lambda z \mathbf{v}; k)\, \tilde{S}(\mathbf{v}, k)\, dk\end{aligned} \tag{8}$$

For a fixed spatial frequency, $\mathbf{v}$, this expression is an inner product in the wavenumber dimension, over the optical passband of the system, between the actual wavenumber content of the source at a certain spatial frequency and a weighting function imposed by the aperture. We denote the wavenumber weighting function at spatial frequency $\mathbf{v}$ as

$$W(k; \mathbf{v}) = C(\lambda z \mathbf{v}; k) = \sum_{n=1}^{N} \sum_{m=1}^{N} C_{n,m}\left(\frac{2\pi z \mathbf{v}}{k}; k \right) \tag{9}$$

where we have written λ as $2\pi/k$. Note that, for a non-trivial segmented aperture, not all the coarray segments at a given wavenumber will include the spatial frequency $\mathbf{v}$ (see Figure 1). In general, many will not include that frequency for any wavenumber, so the weighting function of (9) will only be influenced by some subset of the subaperture correlations in the double sum.

Equation (8) tells us that for a given spatial frequency in a recorded image, we can observe the value of the inner product of the wavenumber content with a known weighting function, determined by the subaperture transmittances. If the subaperture transmittances are controllable at the time of image formation, we can consider the formation of multiple such weighting functions and attempt to solve the resulting system of linear equations for the wavenumber content. In particular, for L observed images, the equations

$$\tilde{I}_q(\mathbf{v}) = \int_K W_q(k; \mathbf{v})\, \tilde{S}(\mathbf{v}, k)\, dk, \quad \text{for } q = 1, \ldots, L \tag{10}$$

can be solved for $\tilde{S}(\mathbf{v}, k)$. This is true even if $\{W_q\}$ is not an orthogonal set of vectors or even a basis, in which case this set of equations could be "solved" in the least squares sense for the projection of $\tilde{S}(\mathbf{v}, k)$ onto the space spanned by $\{W_q\}$. This is the approach taken in Computed Spectroscopy, and the dimension of this space will be of importance to the performance of the method.

If the only adjustment allowed is the optical path length to the image plane, then each subaperture transmittance function in (1) will be of the form

$$\Phi_n(\mathbf{u}; k) = e^{jk D_n}\, \alpha(\mathbf{u} - \mathbf{u}_n) \tag{11}$$

where D_n is the path length deviation from some nominal value, $\mathbf{u}_n$ is the location of the subaperture on the aperture plane and $\alpha(\mathbf{u})$ is a function centered at the origin describing the common transmittance of all the subapertures. (We have assumed that all the subapertures have the same size, shape and apodization, although the analysis could easily be carried out for more general assumptions.) The subaperture cross-correlation functions associated with (11) are

$$\begin{aligned}C_{n,m}(\mathbf{u}; k) &= e^{jk(D_n - D_m)} \int_A \alpha(\mathbf{w} - \mathbf{u}_n)\, \alpha^*(\mathbf{w} - \mathbf{u}_m - \mathbf{u})\, d\mathbf{w} \\ &= e^{jk(D_n - D_m)}\, X(\mathbf{u} - (\mathbf{u}_n - \mathbf{u}_m))\end{aligned} \tag{12}$$

where $X(\mathbf{w})$ is the autocorrelation of $\alpha(\mathbf{u})$, which is located at lag zero, and $(\mathbf{u}_n - \mathbf{u}_m)$ is the lag at which $C_{n,m}(\mathbf{w};k)$ is located. In particular, if the subapertures are uniformly apodized annuli, then the $\alpha(\mathbf{u})$ functions are like that depicted in the top of Figure 1c, and the corresponding $X(\mathbf{w})$ functions are like that depicted in the bottom.

In order to obtain a set of specific simultaneous equations of the form given by (10), we take L distinct panchromatic images, each with a different set of subaperture settings. For the segmented aperture, the qth weight function is associated with a set of selected path lengths $\left\{D_n^{(q)} \quad \text{for } n = 1,\ldots,N\right\}$; the weight function at spatial frequency $\boldsymbol{\nu}$ is given by

$$W_q(k;\boldsymbol{\nu}) = \sum_{n=1}^{N}\sum_{m=1}^{N} e^{jk(D_n^{(q)} - D_m^{(q)})}\; X\left(\frac{2\pi z\,\boldsymbol{\nu}}{k} - (\mathbf{u}_n - \mathbf{u}_m)\right) \tag{13}$$

Note that each term of the weight function sum is composed of an amplitude weight modulated by a segment of a complex exponential with frequency $(D_n^{(q)} - D_m^{(q)})$. In order to solve the equations given by (10) numerically, they must be discretized both in spatial frequency and in wavenumber. In general, this change of representation will incur some discretization error, but for the special case of bandlimited wavenumber content, a condition guaranteed by the bandlimited response of the optical system, the sampling theorem will allow an exact representation in the two spatial dimensions. In spatial frequency, the images are bandlimited by virtue of the fact that the optical system passes only those spatial frequencies allowed by the aperture (for a given wavenumber). In the wavenumber dimension, the required sample rate depends on the variation of the $\left\{W_q(k;\boldsymbol{\nu})\right\}$ with respect to k.

Numerical Approach.

The discretized version of the problem is obtained by using a two-dimensional DFT for the spatial Fourier transform in (7). The DFT is applied to a sampled version of the intensity image, such as would be obtained from an array of detectors on the image plane if the sensor size were small compared to the PSF. For the qth data image, the DFT is

$$\breve{I}_q(\mathbf{n}) = \frac{1}{M^2}\sum_{m_1=0}^{M-1}\sum_{m_2=0}^{M-1}\int_K I_q(m_1\,\Delta x, m_2\,\Delta x; k)\,dk\; e^{j\frac{2\pi}{M}\mathbf{m}^T\mathbf{n}} \tag{14}$$

where $\mathbf{n}=(n_1,n_2)$ and $\mathbf{m}=(m_1,m_2)$ are index vectors with integer components and Δx is the distance between adjacent samples in both coordinate directions on the image plane. The DFT coefficients $\breve{I}_q(\mathbf{n})$ may be approximately related to the Fourier transform $\tilde{I}_q(\boldsymbol{\nu})$ given in (7) by writing a simple quadrature rule for the 2-D Fourier integral in (7) and expressing the result in terms of (14):

$$\breve{I}_q(\mathbf{n}) \cong \frac{\Delta x^2}{M^2}\,\tilde{I}_q\left(\frac{\mathbf{n}}{M\,\Delta x}\right) \tag{15}$$

Using (15), we may write (10) as

$$\frac{M^2}{\Delta x^2}\,\breve{I}_q(\mathbf{n}) = \int_K W_q\left(k;\frac{\mathbf{n}}{M\,\Delta x}\right)\tilde{S}\left(\frac{\mathbf{n}}{M\,\Delta x},k\right)dk, \quad \text{for } q = 1,\ldots,L \tag{16}$$

Note that the integrand of (16) is a point-by-point product between a DFT and a discrete mask function in the discrete spatial frequency domain. Such an operation implements a circular convolution between the mask and the DFT. In this case, the transform of the mask with respect to the spatial frequency variable is a sampled version of the PSF. This circular convolution is a good approximation for the linear convolution of the optical system only in case the PSF is "small". In the context of the computation being described, this inaccuracy in the model will result in ringing around the spatial edges of the reconstructed multispectral image. This ringing will increase with increasing PSF size. In the frequency domain, this ringing appears as a bias added to spatial frequencies near the coordinate axes, and it can be suppressed during processing. The suppression can be implemented as mean subtraction across a pre-determined range of spatial frequencies, and it introduces a slight error at frequencies not associated with the edge effect.

To complete the computation, (16) must be discretized in k, yielding

$$\frac{M^2}{\Delta x^2}\breve{I}_q(\mathbf{n}) = \sum_{p=0}^{P} W_q\left(p\,\Delta k + k_0; \frac{\mathbf{n}}{M\,\Delta x}\right) \int_{K_p} \tilde{S}\left(\frac{\mathbf{n}}{M\,\Delta x}, k\right) dk \tag{17}$$

where Δk is the sample interval in the wavenumber domain, k_0 is the lowest wavenumber in the integration interval K, $P\,\Delta k + k_0$ is the greatest wavenumber in K and K_p is the pth wavenumber bin, centered at $k = p\,\Delta k + k_0$. We require that Δk be small enough so that the $\{W_q\}$ are all approximately constant over any interval of length Δk, and they can be removed from the integral as in (17). This defines a required sample rate in terms of the variation of the wavenumber weight vectors. For an application that imposes a desired sample rate (like hyperspectral imaging), the $\{W_q\}$ should be synthesized so as to satisfy the constant-value constraint for the desired sample rate. The synthesis is performed by choosing the right path lengths, $\left\{D_n^{(q)} \quad \text{for } n = 1, \ldots, N\right\}$.

When all L such inner products are combined into a matrix expression for the $\mathbf{n}^{th}$ DFT coefficient, the result is

$$\breve{\mathbf{I}}_{\mathbf{n}} = \mathbf{W}_{\mathbf{n}}\,\tilde{\mathbf{S}}_{\mathbf{n}} \tag{18}$$

where $\breve{\mathbf{I}}_{\mathbf{n}}$ is an L-component vector whose q^{th} component is $\left[\breve{\mathbf{I}}_{\mathbf{n}}\right]_q = \frac{M^2}{\Delta x^2}\breve{I}_q(\mathbf{n})$, and $\mathbf{W}_{\mathbf{n}}$ is a P-by-L matrix whose $(p,q)^{th}$ element is $\left[\mathbf{W}_{\mathbf{n}}\right]_{p,q} = W_q\left(p\,\Delta k + k_0; \frac{\mathbf{n}}{M\,\Delta x}\right)$, and $\tilde{\mathbf{S}}_{\mathbf{n}}$ is a P-component vector whose p^{th} component is $\left[\tilde{\mathbf{S}}_{\mathbf{n}}\right]_p = \int_{K_p} \tilde{S}\left(\frac{\mathbf{n}}{M\,\Delta x}, k\right) dk$.

In general, the matrix $\mathbf{W}_{\mathbf{n}}$ is neither square nor of full rank. However, using (18) the value of $\tilde{\mathbf{S}}_{\mathbf{n}}$ can be estimated in the least-squares sense using the pseudo-inverse:

$$\hat{\tilde{\mathbf{S}}}_{\mathbf{n}} = \mathbf{W}_{\mathbf{n}}^{\#}\,\breve{\mathbf{I}}_{\mathbf{n}} \tag{19}$$

and $\mathbf{W}_{\mathbf{n}}^{\#}$, can be computed using the singular value decomposition of $\mathbf{W}_{\mathbf{n}}$ [9], so that:

$$\hat{\tilde{\mathbf{S}}}_{\mathbf{n}} = \sum_{i=1}^{R} \frac{\left(\mathbf{u}_{\mathbf{n},i}^{H}\,\breve{\mathbf{I}}_{\mathbf{n}}\right)}{s_{\mathbf{n},i}}\,\mathbf{v}_{\mathbf{n},i} \tag{20}$$

where $s_{\mathbf{n},i}$ is the ith largest singular value of $\mathbf{W}_{\mathbf{n}}$, $\mathbf{u}_{\mathbf{n},i}$ is the ith right singular vector, $\mathbf{v}_{\mathbf{n},i}$ is the ith left singular vector and R is the number of singular values used in the computation. The singular value decomposition (SVD) required to produce these data may be computed by the well-known Golub-Reinsch algorithm [9]. It should be noted that the matrix $\mathbf{W}_{\mathbf{n}}$ is always known prior to data collection, and so the singular value decomposition can be computed beforehand and the singular vectors and singular values stored until they are needed to compute (20). The value of R is important in this computation, and it is not determined by the SVD; it is usually estimated from the SVD data and it can be less than the algebraic rank of $\mathbf{W}_{\mathbf{n}}$.

The final step in the computation is to perform an inverse spatial DFT to the image domain on each wavenumber plane of the data cube constructed by aggregating the estimates of (19). This done, the estimate of the three-dimensional multispectral source is given by

$$\hat{S} = \mathrm{IDFT}_{\mathbf{n}}\left[\hat{\tilde{\mathbf{S}}}_{\mathbf{n}}\right] \tag{21}$$

which is an M-by-M-by-L data cube in the image domain.

4. Rank of the $\mathbf{W}_{\mathbf{n}}$ as a Function of Spatial Frequency.

The resolution of the wavenumber spectral estimate is limited by the number of independent degrees of freedom in the P-component vector $\hat{\tilde{\mathbf{S}}}_{\mathbf{n}}$, which is limited by the rank of $\mathbf{W}_{\mathbf{n}}$, which is turn is limited by its dimensions: P, the size of

the computed solution vector and L, the number of component images. If the solution approach of (20) is adopted, then the number of degrees of freedom is less than or equal to R, the numerical rank of $\mathbf{W_n}$, which can be less than its algebraic rank. In this section, we examine the algebraic and numerical ranks of $\mathbf{W_n}$. We find that the two are equal for most spatial frequencies, but that the numerical rank goes down to unity in a region near the spatial frequency origin, resulting in loss of any wavenumber resolution for the lowest spatial frequencies. The size of this region is governed by the size of the coarray segment of the subapertures, and the effect can be mitigated by using an aperture with a large number of small subapertures.

Algebraic Rank of W_n.

For a sufficient number of observed images, the algebraic rank of the $\mathbf{W_n}$ is limited within the support of the OTF of the longest wavelength by the number of wavenumber bands. Outside this region, but inside the support of the OTF of the shortest wavelength, the rank declines. Outside the support of the OTF of the shortst wavelength, the rank is zero.

Even if the number of observed data images is sufficiently large, the sets of continuous weights $\{W_q\}$ given by (13) will span spaces of limited dimension, and this will limit the rank of the $\mathbf{W_n}$. We can get a rough idea of the dimension of the space spanned by $\{W_q\}$ using the following approximation. If the amplitude terms in (13) did not vary with wavenumber, a Fourier basis could be constructed for every spatial frequency and the observations would give a Fourier series representation of the wavenumber content. If we ignore the amplitude terms, and imagine that all of the redundant coarray segments contribute a modulating term of the same frequency, then we can predict the maximum dimension, d_{max}, of the resulting Fourier wavenumber bases. If we are able to expand the wavenumber spectrum as a finite, complex Fourier series:

$$\widetilde{S}(\mathbf{v}, k) = \sum_{q=-L}^{L} \alpha_q \, e^{\frac{2\pi j q k}{|K|}} \tag{22}$$

where $|K|$ is the length of the wavenumber interval, then we can equate the qth basis function with the weight function implemented by the qth panchromatic image, so that

$$\frac{2\pi q}{|K|} = \left(D_n^{(q)} - D_m^{(q)}\right) \tag{23}$$

Noting that $|K| = \frac{2\pi}{\lambda_{min}} - \frac{2\pi}{\lambda_{max}}$, we have, for the Lth term

$$L = \frac{\lambda_{max} - \lambda_{min}}{\lambda_{max}\,\lambda_{min}} \max\left(D_n^{(q)} - D_m^{(q)}\right) \tag{24}$$

For example, if we wished to image over the visible region, $\lambda_{min} \cong 400\text{ nm}$ and $\lambda_{max} \cong 670\text{ nm}$, and we have $L \cong \max\left(D_n^{(q)} - D_m^{(q)}\right) \big/ 990$, where both sides of the equation are expressed in nanometers. We can interpret this as saying that the number of independent vectors in the partial Fourier basis of (22) is equal to twice the maximum difference between aperture displacements divided by roughly 1000 nm. So, for example, if the maximal difference is 10,000 nm, then the dimension of the basis for the wavenumber content at any spatial frequency will not exceed 20 according to the approximation. As a point of reference, representing the visible region in 20 equal-sized wavenumber bins give an average width of about 13.5 nm in wavelength. In addition, 10,000 nm is smaller than the temporal coherence length of incident sunlight [5].

It is clear that the amplitude weights in (13) can increase the dimension. For example, a weight function with a high frequency could be converted into two orthogonal vectors by multiplying it by two complementary zero/one vectors. The resulting orthogonal vectors might be orthogonal to many vectors to which the original vector was orthogonal (or nearly so). If a large number of small subapertures are used, there will be a great deal of amplitude diversity in the induced weights, some of which is due to partial cancellation of overlapping coarray segments having differing weight frequencies. Simulations have shown that the approximation of (24) is accurate for arrays with small number of subapertures (nine, for example), and that it underestimates the induced dimension in case of a large number of

subapertures (thirty-three, for example). A large number of subapertures will increase the coarray redundancy and so increase the amplitude diversity.

Numerical Rank of W_n.

Next, we note that the modulating term in (13) is the same everywhere in the coarray segment with which it is associated, and that only the amplitude term varies within the segment. We also note that the zero-lag segment is unmodulated, since it corresponds to autocorrelations of the subapertures and the frequency is always zero in such cases (since, obviously, $D_n^{(q)} - D_n^{(q)} = 0$). Finally, we note that the modulating terms are the only ones that can be controlled and made to differ from image to image; the $X\left(\frac{2\pi z\,\mathbf{v}}{k} - (\mathbf{u}_n - \mathbf{u}_m)\right)$ factors are the same for every image, although their combination is controlled by the modulating terms. To highlight this, we can write (13) as

$$W_q(k;\mathbf{v}) = \sum_{n=1}^{N} X\left(\frac{2\pi z\,\mathbf{v}}{k}\right) + \sum_{n=1}^{N}\sum_{\substack{m=1\\ m\neq n}}^{N} e^{jk(D_n^{(q)} - D_m^{(q)})}\, X\left(\frac{2\pi z\,\mathbf{v}}{k} - (\mathbf{u}_n - \mathbf{u}_m)\right) \tag{25}$$

Now the first term in this sum is centered at the spatial frequency origin and is the same for every recorded image. If we look at look at Fig 1, we see that the zero-lag coarray segment, which is the support of the first term in (25), overlaps with many higher-lag segments. In this region the induced weights are always of the same form: a constant vector plus a modulated weight that varies from image to image. Because of the shape of the subaperture autocorrelations, as depicted in Figure 1c, the constant part becomes much larger than the non-constant part as the spatial frequency approaches the origin. The condition number of a matrix $\mathbf{W_n}$ in this region is approximately the ratio of the amplitude (normalizing factor) of the constant vector, which becomes the largest eigenvalue of $\mathbf{W_n}$, to the smallest eigenvalue of the variable part, which gets very small near the origin because the weights of the subaperture correlation functions based on overlapping coarray segments get small near the edge of the coarray segment. Thus, close to the origin, the induced matrices are very poorly conditioned, and their numerical rank is unity in some region around the origin. Note that the matrices in this region can still be of full *algebraic* rank.

5. SIMULATION RESULTS.

In order to illustrate the results of the computations described above, we now give an example using simulated images. Figure 2 depicts three images of the same scene, which is derived from a multispectral simulation performed at Lockheed Martin SSC using the DIRSIG simulation tool developed at Rochester Institute of Technology [10]. The CS simulation depicted in Figure 2 uses 100 panchromatic images, based on a ground truth data cube of 125 wavenumber planes. The reconstructed HSI has 24 wavenumber planes. All of the simulated panchromatic images have PSF's generated by the aperture of Figure 1a with subaperture path lengths designed by the generation and comparison of a large number of random configurations. Figure 2a depicts a color image generated from the ground truth scene, and Figure 2b is a typical panchromatic image (one of 100). A color image generated from the 24-wavenumber reconstruction is shown in Figure 2c. The same maps from wavenumber to RGB were used for Figures 2a and 2c.

The reconstruction shown in Figure 2c is more accurate in regions containing high spatial frequencies than in regions of more low-pass frequency content. This is especially visible near edges, for example the edges of the roofs and of the running track. This is the result of the failure to reconstruct wavenumber spectra near the spatial frequency origin accurately. It is also apparent that the reconstruction seems less blurred than the component panchromatic images. The point spread functions of the data images have exaggeratedly high sidelobes, while the PSF synthesized by the reconstruction algorithm corresponds to a flat, or uniform, OTF. The reconstruction of Figure 2c also shows inaccurate reconstructions near the image edges. The ringing from the DFT approximation of (16) has been suppressed in this reconstruction by mean subtraction in the frequency domain, but some inaccuracy remains. It seems the lowest frequencies of the edge effect have not been suppressed.

Figure 3 presents plots of the true wavenumber spectrum compared to reconstruction at four arbitrary locations in the frequency domain. The "ground truth" spectrum is plotted in red, while the reconstruction is plotted in blue. No smoothing of the reconstructed spectrum is used. The spectrum is complex in the frequency domain, and the phase is plotted in a second box, below the amplitude. The four plots represent a sequence of points, the modulus of whose

spatial frequency decreases with index. That is, Figure 3a represents a higher spatial frequency than Figure 3b, which is in turn higher than Figure 3c, and so on. Figure 3d is a pixel of full algebraic rank near the spatial frequency origin.

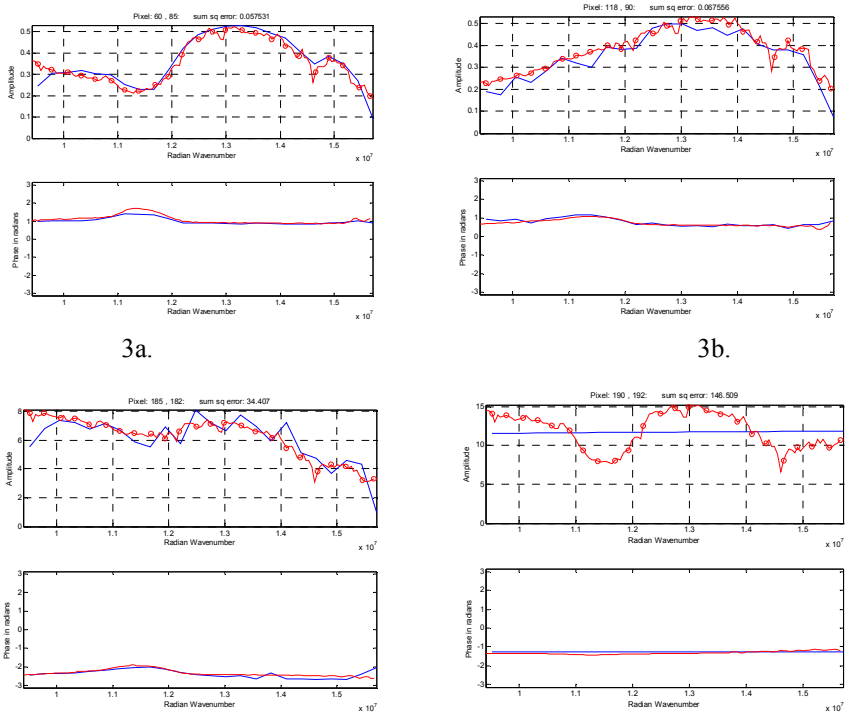

Figure 3: Comparison of true and reconstructed wavenumber spectra for four selected spatial frequencies in the reconstruction depicted in Figure 2c. a: DFT index (60,85); b: DFT index (118,90); c: DFT index (185,182); d: DFT index (190,192).

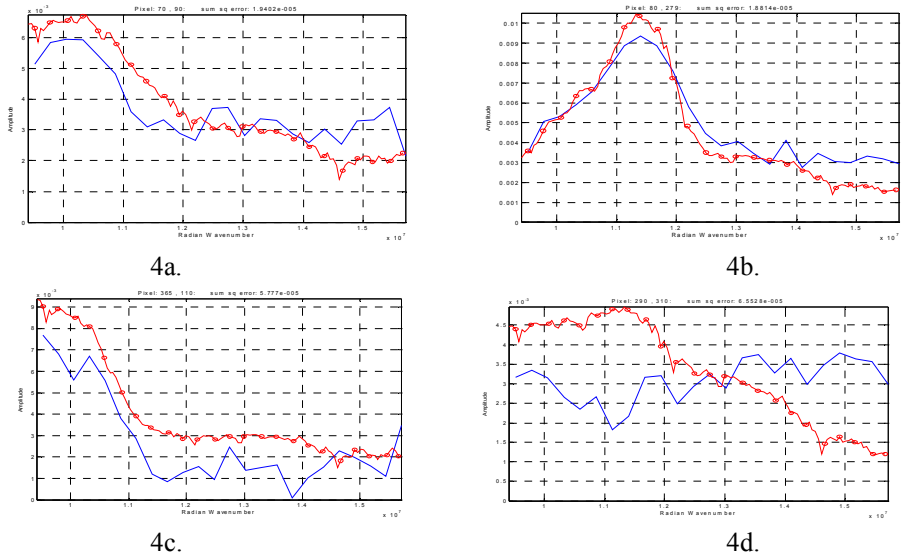

Figure 4: Comparison of true and estimated wavenumber spectra for four selected pixels in the reconstruction depicted in Figure 2c. a: pixel (70,90) – part of brown house roof in upper left; b: pixel (80,279) – green pixel from a tree in upper right; c: pixel (365,110) – part of the red tennis court surround; d: pixel (290,310) – part of the football field.

Comparing the reconstructed spectra in Figure 3, we see that the quality of the reconstruction increases with distance from the origin of the spatial frequency domain. In all cases, the phase has only slight variation with wavenumber, and is well reconstructed. The amplitude is fairly accurately reconstructed for the highest spatial frequency, with increasing error down to the spatial low-pass spectrum, where only the mean value is obtained. This is generally true throughout the spatial frequency domain, but variations in accuracy within a given spatial frequency modulus do occur. Only the DFT coefficient of Figure 3a is completely outside the zero-lag coarray segment.

Figure 4 presents plots of the true wavenumber spectrum compared to reconstruction at four arbitrary locations in the image domain. The "ground truth" spectrum and reconstruction are represented as they are in Figure 3. No smoothing of the reconstructed spectrum is used. The four image pixels are taken from the following identifiable image features: Figure 4a is from a brown house roof in the upper left, Figure 4b is a green pixel from a tree in the upper right, Figure 4c is from the red tennis court surround in the lower left, and Figure 4d is from the green football field. The reconstructed spectra in the image domain are real-valued.

Comparing the reconstructed spectra in Figure 4, we see that none of them is as well reconstructed as the spatial high-pass spectrum reconstruction shown in Figure 3a. Since the error in the low-pass region of the spatial frequency domain is distributed over the whole image, no image points are estimated particularly well even though higher spatial frequencies are estimated well. Those pixels in regions of high spatial frequency energy content are better estimated than those in regions without high spatial frequencies. For example, Figure 4b, which is from an area of very high spatial frequency content, is moderately well estimated. Figures 4a and 4c, which are near edges, are somewhat less well estimated, but have the right basic shape. Figure 4d, on the other hand, which comes from a fairly uniform part of the image, is very poorly estimated.

6. Conclusions and Future Work.

In this paper we have introduced Computed Spectroscopy and given a numerical method for its implementation. We have described CS in the context of a segmented optical aperture, but the approach is applicable to any optical or passive acoustical imagining system for which the PSF can be modified using a broadband, delay-and-sum approach. A simulation of the method for a specific segmented aperture has been performed, and its error characteristics have been explained in terms of the lack of ability to impart a phase weight to the zero-lag coarray segment. Since the size of this low-frequency region is determined by the size of the subapertures, the results of the analysis suggest that segmented apertures with a larger number of smaller subapertures will produce better results than those with small numbers of large apertures. In addition, an algorithmic solution to this problem may be possible [11], but clearly any such approach will work better with a smaller region in which the reconstruction is numerically rank deficient.

Computed Spectroscopy is effectively an aperture synthesis technique in addition to a method for imaging spectroscopy. The point spread function of each image in the computed HSI is that of the "principal solution" narrowband image [6], which has a uniformly weighted OTF and so cannot be produced by a single use of the optical aperture. It can be produced by imaging processing from any narrowband image formed by the aperture, however, which shows that the present subject matter also has a connection to the restoration of images. When attention is restricted to narrowband wavefields, there is a strong similarity between aperture synthesis and image restoration [6], in that both attempt to re-weight the spatial frequency content of the image, one by image addition and the other by two-dimensional filtering. When panchromatic images are considered, however, the PSF is not constant through the image, but rather the spatial variations in wavenumber content cause the PSF to vary spatially. This changes the action required for image restoration from re-weighting of spatial frequency content, which is well-conditioned, to inversion of a spatial varying filter with unknown variations, which is not well-conditioned, in general. We feel that this is the reason that so many image restoration schemes have to make use of regularization functions: it is to deal with the ill-conditionedness that arises from the space-varying PSF of a panchromatic image. Of course, if such processing is done on an imaging spectroscopy data cube, each image plane is nearly monochromatic and the source of ill-conditionedness disappears. The ideas behind the present work draw attention to the fact that there are many connections between incoherent aperture synthesis, spectroscopy and image restoration for both mono- and pan-chromatic images.

The proposed method has some potential advantages over standard methods for imaging spectroscopy. Image plane pan-chromatic intensity sensors record more energy per unit time than sensors in a multispectral imager, because they

respond to the whole visible band. So, for the same SNR and time aperture, it may be possible to acquire a higher spatial resolution image with smaller sensor area. Using computed spectroscopy, this higher image resolution becomes the resolution of the HSI image. Note, however, that the time aperture must include time for acquisition of multiple data images, which may negate the advantage.

In order to synthesize a PSF from multiple apertures, their outputs must be summed coherently, that is, the must interfere with each other. The present technique uses reflected natural light of limited coherence volume, however, so that at some path length difference, interference ceases. This effect limits the maximal path length differences; however, the simulations suggest that hyperspectral imaging is possible without exceeding the coherence limits of the wavefield. This is in contrast to FTIS, which must extend path length differences to the limits of coherence in order to generate a complete interferogram. The SNR at these extreme lags then becomes an issue. The width of the correlation function is inversely related to the width of the spectrum, and in order to adequately reconstruct narrow features, the correlation must be measured at large lags, resulting in a limitation on FTIS resolution. The SNR characteristics of CS have yet to be fully explored and compared to FTIS.

There are several directions in which we hope to proceed with this work. Super-resolution de-aliasing of the individual planes as part of the CS computation will be investigated and a description of FTIS in terms of the CS computational framework would be of value. Simulations have shown a relationship between the spatial resolution of the subaperture array and the required length of the subaperture optical paths that is not explained by the current theory. Finally, we note that the method adopted here for design of a set of path lengths for the panchromatic data set is sub-optimal; we believe that the same results could be achieved with fewer panchromatic images if the design method were improved.

ACKNOWLEDGEMENT

The authors gratefully acknowledge the support of the Lockheed Martin Corporation under the GE Global Research Shared Vision program, and they wish to thank Mr. David Christie of LM-SSC for help with the DIRSIG simulation.

REFERENCES

[1] W.L. Wolfe, *Introduction to Imaging Spectrometers*, SPIE Optical Engineering Press, 1997.

[2] R.L. Kendrick, E.H. Smith and A.L. Duncan, "Imaging Fourier transform spectrometry with a Fizeau interferometer," *Proc. SPIE Interferometry in Space Conference (4852)*, pp. 657-662, August, 2002.

[3] R.L. Kendrick, E.H. Smith, D.N. Christie, D.A. Bennett, D. Theil and E.B. Barrett, "Multiple-aperture imaging spectrometer: computer simulation and experimental validation," *Proc. 33d IEEE Applied Imagery Pattern Recognition Workshop*, pp. 3-9, Oct. 2004.

[4] S.T. Thurman and J.R. Fienup, "Fourier transform imaging spectroscopy with a segmented-aperture telescope or multiple telescope array," *Proc. SPIE Optical, Infrared and Millimeter Space Telescopes (5487)*, June, 2004.

[5] G.O. Reynolds, J.B. DeVelis, G.B. Parrent, and B.J. Thompson, *The New Physical Optics Notebook: Tutorials in Fourier Optics*, SPIE Optical Engineering Press, 1989.

[6] R.T. Hoctor and S.A. Kassam, "The unifying role of the coarray in aperture synthesis for coherent and incoherent imaging," *Proceedings of the IEEE*, vol. 78, pp. 735-752, April, 1990.

[7] D.H. Johnson and D.E. Dudgeon, *Array Signal Processing: Concepts and Techniques*, Prentice-Hall, 1993.

[8] J.W. Goodman, *Introduction to Fourier Optics*, McGraw-Hill, 1968.

[9] G.H. Golub and C.F. Van Loan, *Matrix Computations, 2d Ed.*, Johns Hopkins University Press, 1989.

[10] *The DIRSIG Users Manual*, Digital Image and Remote Sensing Laboratory (DIRS), Rochester Inst. Tech., 2004.

[11] S.T. Thurman and J.R. Fienup, "Reconstruction of multispectral image cubes from multiple-telescope array Fourier transform imaging spectrometer," *Digest Optical Soc. Am. Frontiers in Optics*, paper FTuB3, Oct., 2004.

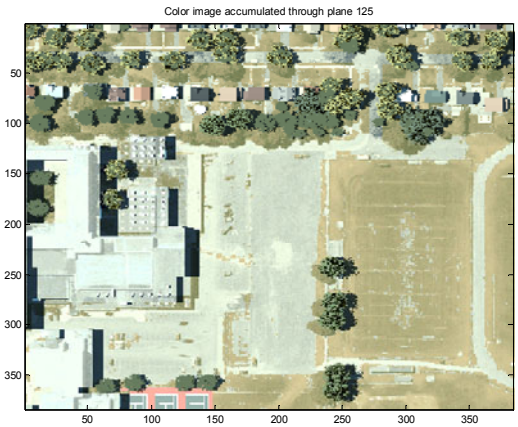

2a.

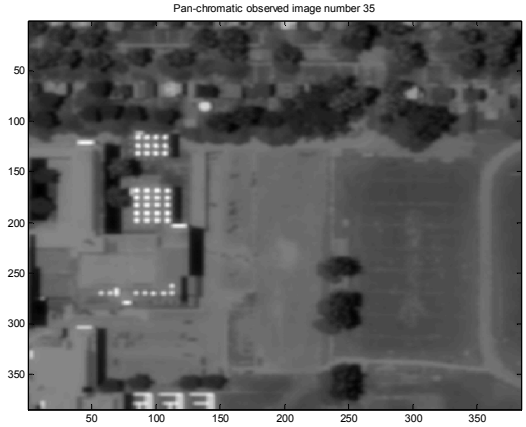

2b.

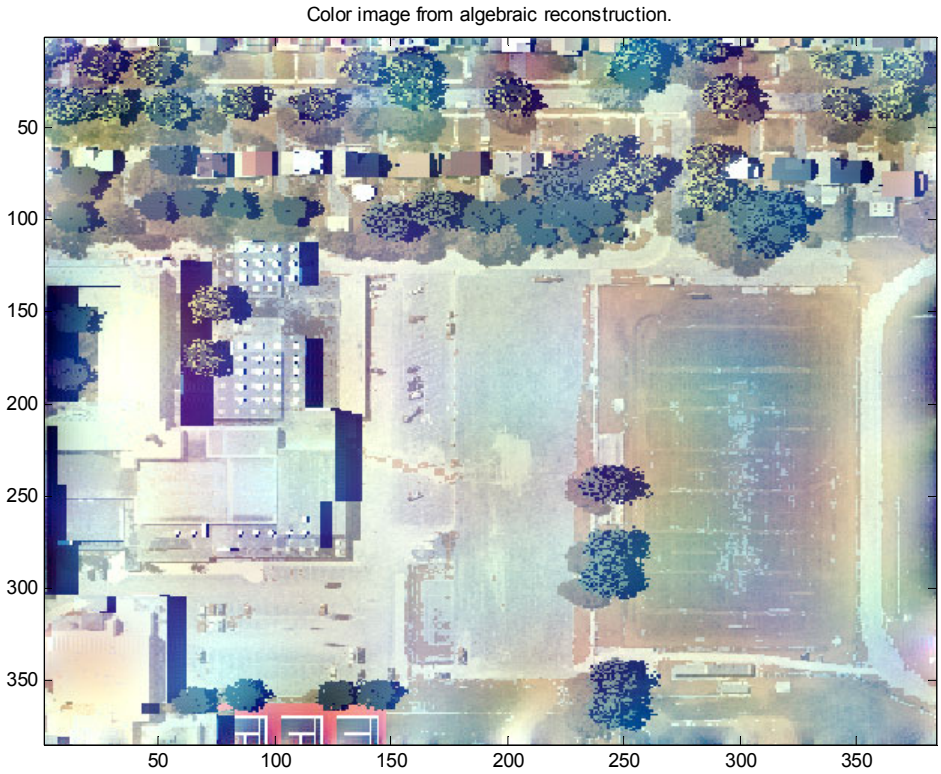

2c.

Figure 2: Ground truth (a) and (b) typical simulated panchromatic image and reconstructed color image (c) from simulation data.